Astronomy & Astrophysics manuscript no. Article
July 6, 2016

Performance of hybrid externally occulted Lyot solar coronagraph

Application to ASPIICS

R. Rougeot[1], R. Flamary[2], D. Galano[1], and C. Aime[2]

[1] European Space Research and Technology Center, European Space Agency, Keplerlaan 1, 2201 Noordwijk , The Netherlands
[2] Laboratoire Lagrange, Universié de Nice Sophia-Antipolis, Centre National de la Recherche Scientifique, Observatoire de la Côte d'Azur, Parc Valrose, 06108 Nice, France

Received ; accepted

ABSTRACT

Context. The future ESA Formation Flying mission Proba-3 will fly the solar coronagraph ASPIICS which couples a Lyot coronagraph of 50mm and an external occulter of 1.42m diameter set 144m before.
Aims. We perform a numerical study on the theoretical performance of the hybrid coronagraph such ASPIICS. In this system, an internal occulter is set on the image of the external occulter instead of a Lyot mask on the solar image. First, we determine the rejection due to the external occulter alone. Second, the effects of sizing the internal occulter and the Lyot stop are analyzed. This work also applies to the classical Lyot coronagraph alone and the external solar coronagraph.
Methods. The numerical computation uses the parameters of ASPIICS. First we take the approach of Aime, C. 2013, A&A 558, A138, to express the wave front from Fresnel diffraction at the entrance aperture of the Lyot coronagraph. From there, each wave front coming from a given point of the Sun is propagated through the Lyot coronagraph in three steps, from the aperture to the image of the external occulter, where the internal occulter is set, from this plane to the image of the entrance aperture, where the Lyot stop is set, and from there to the final observing plane. Making use of the axis-symmetry, wave fronts originating from one radius of the Sun are computed and the intensities circularly averaged.
Results. As expected, the image of the external occulter appears as a bright circle, which locally exceeds the brightness of the Sun observed without external occulter. However, residual sunlight is below $10^{-8}B_\odot$ outside $1.5R_\odot$. The Lyot coronagraph effectively complements the external occultation. At the expense of a small reduction in flux and resolution, reducing the Lyot stop allows a clear gain in rejection. Oversizing the internal occulter produces a similar effect but tends to exclude observations very close to the limb. We provide a graph that allows simply estimating the performance as a function of sizes of the internal occulter and Lyot stop.

Key words. Sun: corona - Instrumentation: high angular resolution - Method: analytic

1. Introduction

The active study of the solar corona governs our knowledge about space weather and stellar atmosphere. Observations in white light requires long observation time in perfect eclipse conditions, because the solar corona is much fainter than the solar disc itself in this spectral band, typically from $10^{-6}B_\odot$ to $10^{-10}B_\odot$ depending on the observed coronal region, where $B_\odot$ is the mean solar brightness (Allen 2005). A very low level of stray light must be achieved, following the requirements about resolution and signal to noise ratio (SNR), and impacting therefore the whole design of the coronagraphic instrument. By creating artificial eclipses, the first Lyot solar coronagraph was a breakthrough for the study of the solar corona (Lyot 1939; Dollfus 1983). Unfortunately, ground-based coronagraphy encounters many limitations such as the significant disturbance from Earth's atmosphere and internal turbulence. The development of the external occultation technique (Evans 1948) coupled with advanced stray light rejection concepts, such as toothed or multiple discs (Newkirk & Bohlin 1965; Purcell & Koomen 1962), and the advent of space-borne coronagraphy enabled to overcome these limitations. As a result, the performance of solar coronagraphs has been considerably improved until 1980s, as described in the review paper by Koutchmy (1988). The successful Solar and Heliospheric Observatory mission including the solar coronagraphs LASCO (Large Angle Spectroscopic Coronagraph) (Brueckner et al. 1995) can be held as a representative and successful example, as it managed to observe the solar corona from $2R_\odot$, where $R_\odot$ is the angular radius of the Sun, by rejecting scattered sunlight at a level of $10^{-10}B_\odot$. However, the detection of fine scale phenomena, as well as sporadic events like Coronal Mass Ejections, asks for even more precise measurements of the radiance at very high angular resolution. Typically, observing the very limb-close solar corona, i.e. below $1.2R_\odot$, where instrumentally scattered sunlight usually predomines, has never been successful without lunar eclipse.

The development of formation flying space mission shall pave the way for new advanced concept of space instrumentation by virtually extending the instrument to unprecedented size, especially for coronagraphy. The solar coronagraph ASPIICS (*Association de Satellites Pour l'Imagerie et l'Interférométrie de la Couronne Solaire*) described by Lamy et al. (2010) and Renotte et al. (2015) takes advantage of the future ESA Formation Flying mission Proba-3. As primary payload, this giant externally occulted coronagraph is split between two spacecraft. A 1.42m diameter occulting disc is mounted on the Occulter Spacecraft while the telescope is carried by the Coronagraph Spacecraft positioned 144m behind. The performance thus results from the

combination of the external occultation of the Sun and the internal Lyot-style coronagraph, with a totally unprecedented large geometry never reached before. The details of the optical design are can be found in Galy (2015). The scientific objectives of ASPIICS are mainly to observe fine scale structure and phenomena very close to the solar limb, from $1.08R_\odot$ to $3R_\odot$, as never has been done, with a spatial resolution of 5.6arcsec. It demands to reject stray light below $10^{-6} - 10^{-7}B_\odot$, which is the level of the coronal brightness at $1.08R_\odot$ (Allen 2005).

As already mentioned, instrumentally scattered light represents one of the main limitation to spaceborne observations. In particular for the solar coronagraphy, the performance is mostly driven by the diffraction of direct sunlight by any occulting masks and any field stops. The fine analysis of this stray light remains very complex and sensitive work, which demands didacated study of extended light source such the Sun. As of now, stray light rejection of past solar coronagraphs has classically been estimated by experimental approaches, like the works described in Fort et al. (1978), Bout et al. (2000), Venêt et al. (2010) and Landini et al. (2010). In contrast, extensive numerical analysis appears nowadays mandatory, or at least complementary, for modern advanced instruments. In this article, we present a dedicated analytic study on the performance of (giant) coronagraphic systems, whose size parameters are those of ASPIICS. As closely related work, an article by Aime (2013) presents the first theoretical performance of sharp-edged or apodized external occulters for solar coronagraphy. We build upon this analysis to present a complete model for the propagation of the wave fronts, and to compute the global response of the externally occulted hybrid Lyot coronagraph such ASPIICS, that we compare to the original Lyot coronagraph and the external solar coronagraph. We also investigate the impact of oversizing the Lyot mask and the impact of reducing the Lyot stop on stray light rejection.

The article is organized as follows. The model and the frame of work adopted for this work are given in Section 2. The mathematical wave propagation into the Lyot-style coronagraph is derived in Section 3, standing as a totally new computation. The comparison of the response of the different coronagraphic systems and further analysis on sizing both internal occulter and Lyot stop are discussed in Section 4. Conclusions are given in Section 5.

2. Model of the coronagraph

2.1. Presentation of the model

The original Lyot coronagraph is made of four remarkable planes representing the instrument. In previous theoretical study of this system by Aime (2002), these planes are denoted as A (entrance aperture), B (focal plane), C (image of the entrance aperture) and D (final focal plane). By adding an external occulter, two additional planes must be introduced. On one hand, the external occulter is positioned in plane O at finite distance before the entrance aperture of the telescope. On the other hand, plane O' denotes the image of the external occulter made by telescope. It is located further behind the focal plane. The following list recalls the names and descriptions of all the planes, also illustrated in Figure 1.

Plane O External occulter plane, as a sharp-edged perfect disc.
Plane A Aperture of the telescope. We assume that the primary objective (L1) coincides with the pupil.
Plane B Focal plane of the telescope.
Plane O' Image plane of the external occulter made by the telescope.
Plane C Image of the entrance aperture. The Lyot stop and the third objective (L3) are set here.
Plane D Final focal plane of the instrument for detection.

The light encounters these successive planes in order O, A, B, O', C and D. In our work, we study three different coronagraphic systems plus the related reference imaging system:

$S_\emptyset$ Raw telescope used as a reference, made of plane A and plane B.
S_L Original Lyot coronagraph including the Lyot mask in plane B, and the Lyot stop in plane C.
S_E External solar coronagraph including the external occulter in plane O only, and ending at the focal plane B.
S_{EL} Externally occulted hybrid coronagraphic system composed of the external occulter in plane O, the internal occulter and the second objective (L2) in plane O', and the Lyot stop in plane C.

We intentionally chose to respect the following naming convention. The Lyot mask denotes the occulter set in plane B, according to the original Lyot coronagraph. The internal occulter denotes the second occuting disc set in plane O' for the hybrid coronagraphic system S_{EL}, corresponding to the Lyot mask in this particular case. This article presents and compares the global response of these four systems, but it will focus on the hybrid coronagraphic system S_{EL}, as it consists of a totally new computation. The four systems $S_\emptyset$, S_L, S_E and S_{EL} include the same circular entrance aperture in plane A. their schematic representations are given in Figure 1.

Our model is generic. However, the parameters of the numerical experience are those of ASPIICS. The external occulting disc of radius $R = 710$mm is located at $z_0 = 144.348$m before the 50mm diameter entrance aperture. The telescope consists of a converging lens of focal length $f = 330.385$mm. The Sun is legitimately assumed to be at infinity. Its angular radius is $R_\odot = 0.0046542$rad as seen from the centre of the aperture, so ~ 16.2arcmin. As viewed from the telescope aperture, the external occulter already masks up to $1.0568R_\odot$ at the center of the pupil - $1.0196R_\odot$ with 100% vignetting and $1.094R_\odot$ with 0% vignetting. Table 1 summarizes the numerical parameters.

The radius of the Lyot mask set in plane B will be given in solar units $R_\odot$, since this plane is the conjugate of the solar disc. However, the internal occulter is set in plane O' which is the conjugate image of plane O. We will thus speak in terms of units of external occulter image. A simple proportional relationship applies here to convert this particular units system to solar units, or metric units. In plane O', the image of R corresponds to 1.629mm and to $1.0568R_\odot$, as given in Table 1. We emphasize that using solar unit has no real meaning to plane O', since it is not conjugated with the Sun.

2.2. Analytic frame of work

All the planes previously defined are assumed to be perfectly parallel and aligned with respect to the optical axis, so that the geometry is axis-symmetric. The impact of a tilt or an off-set would in itself deserve further analysis but it is left to future works. To each plane we set a r, θ, z cylindrical coordinate system. The z-axis refers to the optical axis, oriented positively towards the detection plane. The corresponding Cartesian coordinate system (x, y, z) is defined by $x = r\cos\theta$ and $y = r\sin\theta$.

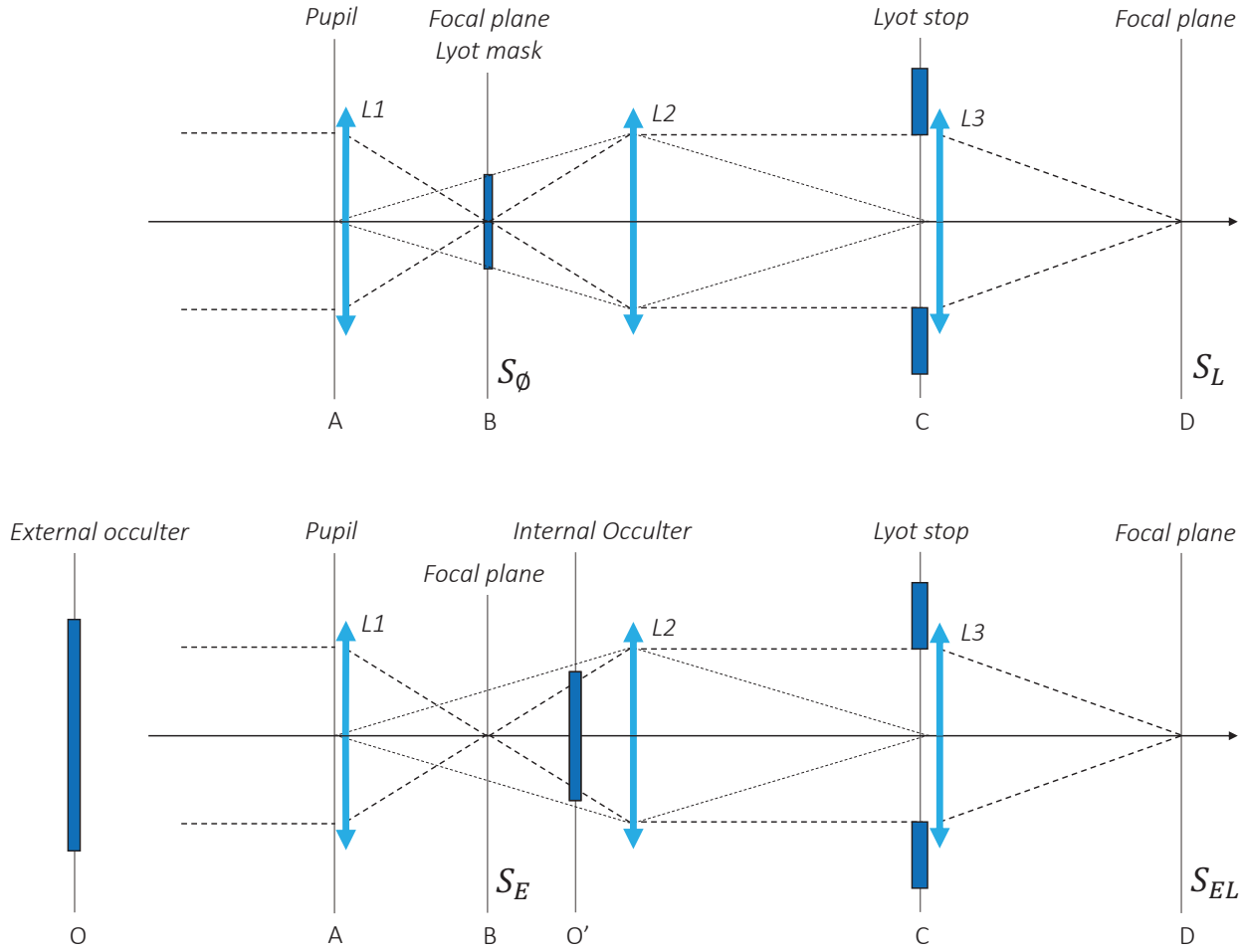

Fig. 1. Schematic representation of the four coronagraphic systems. Top: the original Lyot coronargaph S_L made of planes A, B, C and D. The raw telescope $S_\emptyset$ ends at focal plane B, i.e. without Lyot coronagraph. Bottom: the externally occulted hybrid Lyot coronargaph S_{EL} made of planes O, A, O', C and D. The external solar coronagraph S_E ends at focal plane B. Figures not to scale.

In the remaining of the article, we will sometimes use both coordinates simultaneously, because this slight abuse of notation allows more compact and readable equations. To provide a better understanding, we will use as subscript the letter O, A, B, O', C or D referring to the corresponding plane for every quantity.

Our study uses monochromatic light, here $\lambda = 550$nm. We adopt Fresnel regime to describe diffraction induced by the external occulter, as suggested by the large value of Fresnel number $\mathcal{N}_f = R^2/\lambda z_0 = 6350$ (Born & Wolf 2006). To model the perfect sharp-edged disc, the transmission in plane O is a radial gate function $\tau(r) = 0$ if $r \leq R$ and $\tau(r) = 1$ else. The pupil of the telescope is a perfect circular entrance aperture of radius $R_p = 25$mm.

The analytic propagation of wave front is based on paraxial Fourier optics formalism (Goodman 2005). Under this assumption, Fresnel free-space propagation of a wave front $\Psi_0(x,y)$ over a distance z is written as convolution product. The complex amplitude $\Psi_z(x,y)$ of the propagated wave front at distance z is

$$\begin{aligned}\Psi_z(x,y) &= \Psi_0(x,y) \circledast \frac{1}{i\lambda z}\exp\left(i\pi\frac{x^2+y^2}{\lambda z}\right) \\ &= \frac{\varphi_z(r)}{i\lambda z} \times \mathcal{F}_{\lambda z}\left[\Psi_0(x,y) \times \varphi_z(r)\right] \end{aligned} \quad (1)$$

where $\varphi_z(r) = \exp(i\pi r^2/\lambda z)$ and $r = \sqrt{x^2+y^2}$ is the transverse radius in cylindrical coordinates. $\mathcal{F}_{\lambda z}$ denotes the 2D Fourier transformation with spatial frequencies $u = x/\lambda z$ and $v = y/\lambda z$. Eq.(1) is the so-called Fourier-Fresnel transformation of the function $\Psi_0(x,y)$, where the phase term $\exp(2i\pi z/\lambda)$ for the longitudinal propagation has voluntary been omitted. Moreover, in the Fourier formalism, a converging lens of focal length f is modeled by the quadratic phase factor $\varphi_{-f}(r) = \exp(-i\pi r^2/\lambda f)$. Propagating through a lens consists of multiplying the complex amplitude of the incoming wave front by $\varphi_{-f}(r)$. A well known result is the propagation to the focal plane of a lens, i.e. $z = f$ in Eq.(1). In this case, both quadratic phase factors $\varphi_{-f}(r)$ and $\varphi_{+f}(r)$ cancel each other. Consequently, the wave in the focal plane is directly proportional to the Fourier transformation of the incoming wave at its entrance, with to a scale factor λf and a quadratic term $\varphi_f(r)$ that vanishes when computing the related intensity.

The Sun is modeled by a collection of incoherent point sources. The global response of any system is given by the incoherent sum of their respective elementary intensities. Every point source is identified by a set of angular coordinates (α,β) on the sky, with $\sqrt{\alpha^2+\beta^2} \leq R_\odot$. To provide a better understanding, we will also use as subscripts the coordinates (α,β) to refer

Table 1. Parameters used to model the four coronagraphic systems. See text for details.

Parameter	Value
Wavelength	$\lambda = 550$nm
Angular radius of the Sun	$R_\odot = 0.0046542$rad
Distance to the Sun	∞ (1 Astronomical Unit)
Radius of the external occulter	$R = 710$mm
Distance plane O - plane A	$z_0 = 144.348$m
Radius of the pupil	$R_p = 25$mm
Focal length of the telescope	$f = 330.385$mm
Image of R in plane O'	1.629mm
	$1.0568 R_\odot$

to a precise point source for every quantity. As the Sun is at infinity, the light coming from every points source is modeled by tilted planar wave, whose unitary complex amplitude is written as $\Psi_{\odot,\alpha,\beta}(x,y) = \exp(-2i\pi/\lambda(\alpha x + \beta y))$.

We use the center-to-limb variation of the Sun $B(\alpha,\beta)$ from Hamme (1993). This choice has been driven by the need to have a representative limb darkening function for the wavelength $\lambda = 550$nm. Other functions may be used, but would require new numerical computations. Still we believe that another function would only slightly change the results.

$$B(\rho) = 1 - 0,762\left(1-\sqrt{1-\rho^2}\right) - 0,232\left(1-\rho^2\right)\log\left(\sqrt{1-\rho^2}\right) \quad (2)$$

where $\rho = \sqrt{\alpha^2+\beta^2}/R_\odot$ is expressed in solar unit.

2.3. Fresnel diffraction by the external occulter

Fresnel diffraction produced by a sharp-edged disc has already been fully described by Aime (2013) (his Eq.(5)). The tilted planar wave front $\Psi_{\odot,\alpha,\beta}(x,y)$ coming from the point source at (α,β) arrives onto the occulting disc in plane O, and then propagates following the Fourier-Fresnel transformation. Related complex amplitude $\Psi_{A,\alpha,\beta}$ of the wave front arriving on plane A is thus

$$\begin{aligned}\Psi_{A,\alpha,\beta}(x,y) &= \left[\Psi_{\odot,\alpha,\beta}(x,y)\times\tau\right] \circledast \frac{1}{i\lambda z_0}\exp\left(i\pi\frac{x^2+y^2}{\lambda z_0}\right) \\ &= T_{\alpha,\beta}(x,y)\times\Gamma_{\alpha,\beta}\times\Psi_{A,0,0}(x+\alpha z_0, y+\beta z_0) \quad (3)\end{aligned}$$

where

$$T_{\alpha,\beta}(x,y) = \exp\left(-2i\pi\frac{\alpha x+\beta y}{\lambda}\right) \quad \text{(Tilt)}$$

$$\Gamma_{\alpha,\beta} = \exp\left(-i\pi\frac{(\alpha^2+\beta^2)z_0}{\lambda}\right) \quad \text{(Offset)}$$

$$\Psi_{A,0,0}(x,y) = 1 - \frac{1}{i\lambda z_0}\iint_{\eta^2+\xi^2\le R^2}\exp\left(i\pi\frac{(x-\xi)^2+(y-\eta)^2}{\lambda z_0}\right)d\xi d\eta \quad (4)$$

with ξ,η the Cartesian variables for integration over the occulting disc. As a result, an off-axis point source produces the same complex amplitude as the on-axis point source, i.e. $\Psi_{A,0,0}$, but shifted of the quantity $(z_0\times\alpha, z_0\times\beta)$ towards negative (x,y) directions. The constant phase term $\Gamma_{\alpha,\beta}$ accounts for the offset of position, and the original tilt $T_{\alpha,\beta}$ of the wave is conserved. Let us now consider the particular case of the on-axis point source. Taking advantage of the cylindrical symmetry, we naturally change

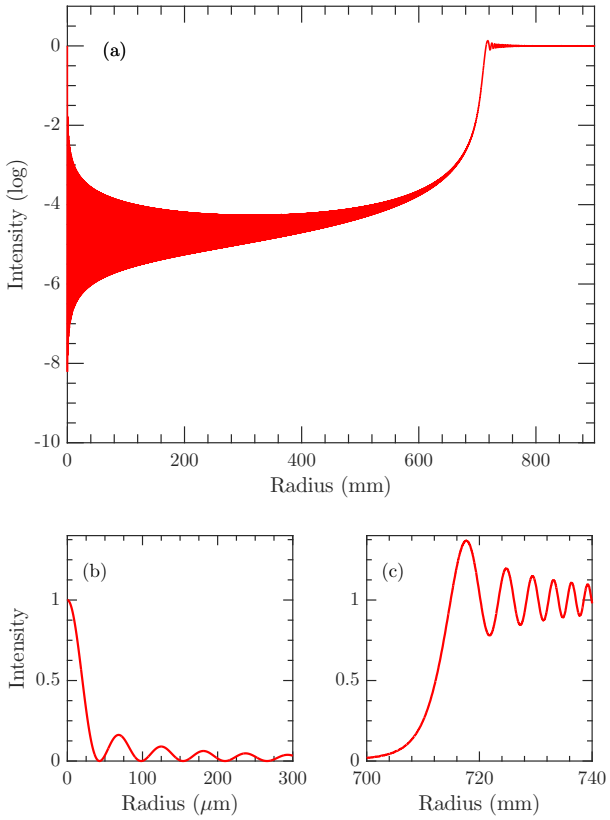

Fig. 2. Fresnel diffraction pattern $|\Psi_{A,0,0}(r)|^2$ for unitary on-axis point source at infinity, for the 710mm radius disc at $z_0 = 144.348$m. (a) Full range, in logarithmic scale. (b) Zoom in Arago bright spot at the central region $[0, 500\mu$m], in linear scale. (c) The transition region between shadow and light around 710mm, in linear scale.

for polar coordinates (r,θ). Eq.(4) is then written as a radial Hankel transformation, as given in Eq.(11) of Aime (2013):

$$\Psi_{A,0,0}(r) = 1 - \frac{\varphi_{z_0}(r)}{i\lambda z_0}\int_0^R 2\pi\rho\exp\left(i\pi\frac{\rho^2}{\lambda z_0}\right)J_0\left(2\pi\frac{r\rho}{\lambda z_0}\right)d\rho \quad (5)$$

where ρ is the radial variable for integration over the disc, r is the transverse radial coordinate on plane A, $\varphi_{z_0}(r) = \exp(i\pi r^2/\lambda z_0)$ and $J_0(r)$ is the Bessel function of the first kind. Eq.(5) is the exact analytic expression of Fresnel diffraction in the particular case of the on-axis point source. From a numerical point of view, this integral requires huge computation time because the numerical step-size $d\rho$ must be of the order of λ to be consistent. An analytic expression using Lommel series can alternatively be used, as proved by Aime (2013), and the interest reader is referred to this work. Figure 2 (curve (a)) illustrates Fresnel diffraction pattern $|\Psi_{A,0,0}(r)|^2$, known as the bright spot of Arago, for the 710mm diameter disc at the distance $z_0 = 144.348$m, in a logarithmic scale. A very high spatial sampling of 0.1μm in plane A has been used. Figure 2 also shows the central spot in linear scale (curve (b)), whose peak amplitude is 1 for $r = 0$ as expected, and the transition zone between shadow and light (curve (c)). Note that the amplitude decreases below 10^{-4} for larger values of r.

3. Propagation through the coronagraph

The propagation of every incoming wave front through each successive planes of the coronagraph is a coherent process. However, the observed response is the result of an incoherent summation of elementary intensities, meaning that every point source composing the Sun can be treated individually. So, let us consider one point source located at (α, β) in the sky. We analytically write this coherent process of wave propagation, accordingly with each system $S_\emptyset$, S_L, S_E or S_{EL}. The complex amplitude of the wave fronts Ψ_B, $\Psi_{O'}$, Ψ_C and finally Ψ_D are successively computed, by starting from $\Psi_{A,\alpha,\beta}$, which will be denoted as Ψ_A for better readability. From here, the polar coordinates (r, θ) are preferred to the Cartesian coordinates (x, y).

3.1. Classic Lyot coronagraph

As already described, the original Lyot coronagraph S_L is modeled by planes A, B, C and D (Aime 2002), and does not include the external occulter. The incoming wave front Ψ_A at the entrance aperture simply consists of the tilted planar wave front. Here, the coronagraph acts as a mere imaging system, adding the Lyot mask in plane B, i.e. the focal plane. Using the approach of Fourier formalism described in Sec.2.2, the propagation process through the whole instrument consists of scaled Fourier transformations between each of the successive planes, i.e. from A to B, from B to C and from C to D. The images are of different sizes, depending on the lenses used for imaging, but these differences in size do not affect the result. In terms of Fourier analysis, the Lyot mask in B behaves as a high pass filter and the Lyot stop in C behaves as a low pass filter. It is the conjugate effect of these two masks that makes the Lyot coronagraph efficient for the rejection of the direct sunlight where we want to observe the corona.

We name $\mathcal{P}(r)$, $\mathcal{M}(r)$ and $\mathcal{L}(r)$ the radial transmission functions of the entrance pupil in A, the Lyot mask in B and the Lyot stop in C respectively. The wave front Ψ_B is computed from the Fourier-Fresnel transformation, as given in Eq.(1)

$$\Psi_B(r,\theta) = \frac{\varphi_f(r)}{i\lambda f} \times \widetilde{\Psi}_B(r,\theta) \tag{6}$$

where $\widetilde{\Psi}_B(r,\theta) = \mathcal{F}_{\lambda f}\left[\Psi_A(r,\theta) \times \mathcal{P}(r)\right]$. We remind that the quadratic phase term $\varphi_f(r)$ vanishes when computing related intensity. The wave front in plane B encounters the Lyot mask $\mathcal{M}(r)$ and the second objective L2 of focal f_2. Plane C is the image plane of the entrance aperture that is located at a distance $d = f \times f_2/(f - f_2)$ from plane B, as given by the relation of conjugation for lens. Writing again a Fourier-Fresnel transformation of Ψ_B over the distance d, the three quadratic phase factors $\varphi_f(r)$, $\varphi_{-f_2}(r)$ and $\varphi_d(r)$ cancel each other.

$$\begin{aligned}\Psi_C(r,\theta) &= \frac{\varphi_d(r)}{i\lambda d} \times \mathcal{F}_{\lambda d}\left[\Psi_B(r,\theta) \times \mathcal{M}(r) \times \varphi_{-f_2}(r) \times \varphi_d(r)\right] \\ &= \frac{-\varphi_d(r)}{\lambda^2 f d} \times \widetilde{\Psi}_C(r,\theta)\end{aligned} \tag{7}$$

where $\widetilde{\Psi}_C(r,\theta) = \mathcal{F}_{\lambda d}\left[\widetilde{\Psi}_B(r,\theta) \times \mathcal{M}(r)\right]$. Again, the intensity in plane C is simply proportional to the Fourier transformation of $\widetilde{\Psi}_B\,(r,\theta) \times \mathcal{M}(r)$ (Aime 2002). Based on the same principle, the wave front in plane D is then obtained by performing a Fourier transformation of $\widetilde{\Psi}_C(r,\theta) \times \mathcal{L}(r)$, corresponding to the image on the focal plane of the whole imaging system.

$$\Psi_D(r,\theta) = \frac{\varphi_f(r)}{i\lambda f} \times \mathcal{F}_{\lambda f}\left[\widetilde{\Psi}_C(r,\theta) \times \mathcal{L}(r)\right] \tag{8}$$

In a similar way, the wave propagation for the reference telescope $S_\emptyset$ is limited to the first propagation to plane B, i.e. Eq.(6). We also used this analytic formulation for the external solar coronagraph S_E by considering Fresnel diffraction for the complex amplitude Ψ_A at the entrance aperture, expressed by Eq.(3).

3.2. Externally occulted coronagraphic system

Let us now consider the externally occulted hybrid Lyot coronagraph S_{EL}. This system varies from the classic Lyot coronagraph S_L, since it includes the internal occulter set in plane O'. Plane B has no more actual interest in this particular case and shall be skipped. Moreover, Ψ_A consists now of Fresnel diffracted wave front as given in Eq.(3), because of the external occulter in plane O. We directly write the Fourier-Fresnel propagation over the distance $z_1 = z_0 f/(z_0 - f)$ between planes A and O'. The wave front $\Psi_{O'}$ in plane O' is then expressed as

$$\begin{aligned}\Psi_{O'}(r,\theta) &= \frac{\varphi_{z_1}(r)}{i\lambda z_1} \times \mathcal{F}_{\lambda z_1}\left[\Psi_A(r,\theta) \times \mathcal{P}(r) \times \varphi_{-f}(r) \times \varphi_{z_1}(r)\right] \\ \Psi_{O'}(r,\theta) &= \frac{\varphi_{z_1}(r)}{i\lambda z_1} \times \widetilde{\Psi}_{O'}(r,\theta)\end{aligned} \tag{9}$$

where $\widetilde{\Psi}_{O'}(r,\theta) = \mathcal{F}_{\lambda z_1}\left[\Psi_A(r,\theta) \times \mathcal{P}(r) \times \varphi_{-z_0}(r)\right]$. The main difference between $\widetilde{\Psi}_B$ and $\widetilde{\Psi}_{O'}$, in Eq.(6) and Eq.(9) respectively, is the quadratic phase factor $\varphi_{-z_0}(r) = \exp(-i\pi r^2/\lambda z_0)$. It can be seen as a virtual converging lens of focal length z_0 which rejects the external occulter at infinity. Consequently, the following image of plane O made by the primary objective is now moved into the focal plane, and so it is computed as a simple Fourier transformation, as previously. This reasoning makes the computations much simpler than considering the wave in plane B and propagating it to O' with a Fresnel propagation over the distance $f^2/(z_0 - f)$.

Then, the wave front in plane O' encounters the internal occulter $\mathcal{M}(r)$ and the second objective L2. We can thus directly apply Eq.(7) to derive the complex amplitude of the wave front in plane C, where the distance d refers now to $d = z_1 \times f_2/(z_1 - f_2)$. However, the quadratic phase factor $\varphi_{-z_0}(r)$ remains. Since we want to obtain in plane C the image of the pupil, we have to get rid of this unwanted factor. This is simply obtained by multiplying the complex amplitude in plane C by $\varphi_{+z_0}(r)$, which corresponds to a diverging lens of focal z_0 that compensates the first virtual converging lens.

$$\Psi_C(r,\theta) = \frac{-\varphi_d(r)}{\lambda^2 z_1 d} \times \widetilde{\Psi}_C(r,\theta) \times \varphi_{+z_0}(r) \tag{10}$$

where $\widetilde{\Psi}_C(r,\theta) = \mathcal{F}_{\lambda d_2}\left[\widetilde{\Psi}_{O'}(r,\theta) \times \mathcal{M}(r)\right]$. Finally, the wave front in plane D is given by Eq.(8). To summarize, adding a virtual converging lens of focal length z_0 in plane A and a diverging lens of the same focal length in plane C makes the numerical computation much more convenient and handy.

3.3. Observed intensities

The total intensity I_i on plane $i = \{A, B, O', C, D\}$ is the incoherent sum of the elementary intensities due to every points source describing the whole solar disc. From this section, the complex amplitude $\Psi_{i,\alpha,\beta}\,(r,\theta)$ will be written as a function of four variables $\Psi_i(\alpha, \beta, r, \theta)$, to clarify the integration process. Taking into account the center-to-limb darkening function $B(\alpha, \beta)$, the integrated intensity due to the full Sun is

$$I_i(r,\theta) = \iint B(\alpha,\beta) \times |\Psi_i(\alpha,\beta,r,\theta)|^2 \, d\alpha d\beta \tag{11}$$

where $i = \{A, B, O', C, D\}$. This Fredholm integral of the first kind cannot be computed as a mere convolution since $\Psi_i(\alpha, \beta, r, \theta)$ is not shift invariant with respect to (α, β), and a 2D numerical summation must be performed. But we can actually take advantage of the axis-symmetry of the system. We remind that it assumes that the Sun and every remarkable planes are parallel and aligned to the optical axis. We now replace solar angular coordinates (α, β) by (ρ, θ_s), with $\alpha = \rho \cos\theta_s$ and $\beta = \rho \sin\theta_s$, meaning having $\rho \in [0, R_\odot]$ and $\theta_s \in [0, 2\pi[$. The assumed symmetry makes the 2D image of one point source $|\Psi_i(\rho, \theta_s, r, \theta)|^2$ in plane i rotate identically with respect to the point source on the solar disc, i.e. θ_s. In other words, it only depends on the relative angular difference $\phi = \theta - \theta_s$. As a result, integrating over the solar polar angle θ_s is equivalent to circularly integrating on the 2D image plane, so over θ. Moreover, the solar brightness is a radial function, so $B(\alpha, \beta) = B(\rho)$. By substituting θ by ϕ, the integrated intensity given in Eq.(11) becomes the following radial function

$$I_i(r) = \int_0^{2\pi} \left[\int_0^{R_\odot} B(\rho) \times |\Psi_i(\alpha, \beta, r, \phi + \theta_s)|^2 \rho d\rho \right] d\phi \tag{12}$$

From a numerical point of view, it is much more convenient to compute this last integral than the rough full two dimension integration. In Eq.(12), θ_s can arbitrary be fixed to 0, since the integration is performed over 2π. So we choose $\alpha = \rho$ and $\beta = 0$. This means that we only need to propagate the wave fronts coming from one elementary radius of the Sun. To summarize, we first compute Fresnel diffraction $\Psi_{A,0,0}$ related to the on-axis point source (Eq.(5)). Second, we derive $\Psi_A(\rho, 0, r, \phi)$ as given in Eq.(3)

$$\Psi_A(\rho, 0, r, \phi) = T_{\rho,0}(r, \phi) \times \Gamma_{\rho,0} \times \Psi_{A,0,0}\left(r_{eq}\right) \tag{13}$$

where $r_{eq} = \sqrt{(r\cos\phi + \rho z_0)^2 + (r \sin\phi)^2}$. Third, we propagate the wave front to compute $\Psi_i(\rho, 0, r, \phi)$. Finally, we perform the integration in Eq.(12) as a weighted sum of two dimension images, followed by a circular average of the result.

4. Analysis and discussion

4.1. Numerical implementation

We now present the results of the complete computation of the observed intensities $I_i(r)$ on each plane $i \in \{A, B, O', C, D\}$, accordingly for each configuration $S_\emptyset$, S_L, S_E and S_{EL}. The complex amplitude Ψ_A of the wave front in plane A has been computed in Mathematica (Wolfram 2012). The numerical integration of the Hankel transformation (Eq.(4)) remains a delicate operation, as described by Lemoine (1994). Then, the wave fornt is linearly interpolated and the propagation is performed using Matlab 2D Fast Fourier transformation combined with the recentering routine `fftshift` when necessary. We will provide the reader a complete Matlab/Octave toolbox that will be able to reproduce the following computations for the sake of reproducible research.

A difficult and sensitive parameter in the numerical experiments is the choice of the sampling in each plane. Indeed, as discussed in Soummer (2007), in successive planes, i.e. A to B or A to O', B to C or O' to C and C to D, the sampling requirements are opposite. This problem is known as the two-fold sampling requirement. The point of view which has been adopted in the present work is somewhat empirical. We imposed the same number of points in the occulter image in plane O' and in the telescope aperture in plane A. Note that this *a priori* is sensible since it provide a similar resolution in all planes, but other sampling strategies might be of interest. The telescope aperture is padded inside an array of $N \times N$ points, and $n_p < N$ points are used in the radius R_p of the aperture. The spatial sampling in plane A is thus $s_A = R_p/n$, for a total field $F_A = N \times R_p/n$. Due to the properties of Fourier spatial frequencies, the field F_A in plane A produces a sampling $s_{O'} = \lambda d/F_A$ in plane O', where $d = z_0 f/(z_0 - f)$ is the distance between plane A and plane O'. Moreover, the size of the image radius of the external occulter is $R \times d/z_0$. Therefore, the number of points n_i in the radius of the occulter image is $p = Rd/z_0 s_{O'}$. By imposing $n_i = n_p$, we obtain:

$$n_i = \sqrt{\frac{R \times R_p \times N}{z_0 \times \lambda}} \sim 14.9525\sqrt{N} \tag{14}$$

For numerical reasons, N should preferably be a power of 2, and at least 4096 points are required for a correct sampling of the image to respect Shannon criteria. Of course, the larger N the better the result due to zero-padding effect, being a compromise between computation time and precision.

The results of computation reported in this paper has been made using a machine with two 14 core Intel Xeon processors and 512GB of RAM, using $N = 2^{13} = 8192$ and $n_p = 1353$, meaning that the sampling in plane A is about 18.5μm and the field of about 15.6cm. Each step in the numerical computation has been verified in particular with point sources. We used a Lyot mask or internal occulter of $1.065R_\odot$ radius and a Lyot stop of 24.75mm radius to illustrate the numerical experience, and this should not skew the global results.

4.2. Impulse response in the Lyot coronagraph

We investigate the impulse response of a wave front originating from one point source alone in both plane B and O', including the external occulter set 144.348m before. We first analyzed the case of the on-axis point source. The image produced is a bright perfect circle which fits the image of the external occulter edge. The intensity is very focused in plane O' as expected, illustrated in Figure 3. In this case, the response is perfectly symmetric. We secondly analyzed an off-axis point source at $\alpha = 768$arcsec, i.e. $0.8R_\odot$. Figure 4 shows the two dimension intensities in both plane B and O'. A first interesting result consists of the shift of the image of the Arago spot. Indeed, strongly asymmetric light structures appear, while the on-axis case was perfectly symmetric. The sharpness and the fine scale structure of the diffraction features, visible in the zoom regions in Figure 4, prove the need of a very high sampling on both plane B and O'. Finally, observing the difference between plane B and O' is a very dominant point. Here, the light pattern in plane B tends to be spread along the x-axis, so perpendicularly to the local edge of the image of the external occulter modeled by the y-axis. The light appears out-of-focused. In the contrary, plane O' shows a diffracted light pattern fitting locally the image of the external occulter.

4.3. Response of the different coronagraphic systems

4.3.1. Intensity in plane A

The performance of the external occulter can first be assessed by computing the intensity $I_A(r)$ at the entrance aperture of the telescope. Figure 5 plots the penumbra profile of diffracted light (red curve) and the corresponding geometrical umbra profile (black dashed curve). The horizontal axis represents the radial

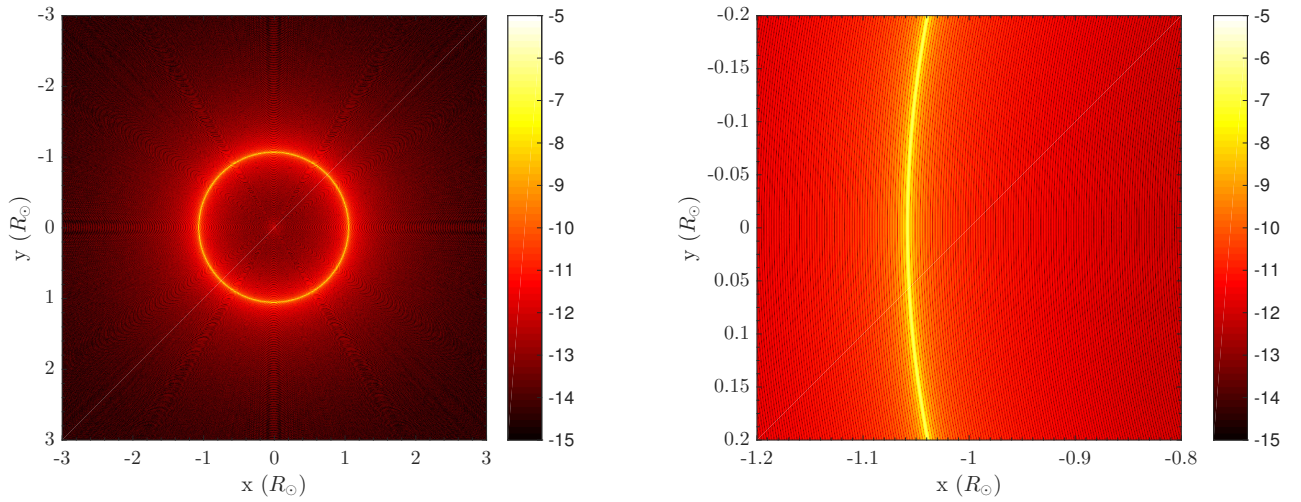

Fig. 3. Two dimension observed intensity in plane O' of diffracted wave front originating from the on-axis point source at the center of the Sun, in logarithmic scale.

coordinate in mm, starting at the center of the umbra cone. The sharp-edged 710mm radius occulter is 1.0568 larger than the solar stenope image, which corresponds to a geometrical umbra of $R - z_0 \tan R_\odot = 38$mm radius. The full solar irradiance statrs at a radius of $R + z_0 \tan R_\odot = 1382$mm, as expected. Because of diffraction, the scattered light remains at a level of $10^{-4} B_\odot$ at the center of the umbra cone, as a flat plateau. The external occulter reduces direct sunlight by a factor of the order 8000 at the entrance aperture of the telescope, which is a first significant advantage for both externally occulted systems S_E and S_{EL}. Here, apodization techniques (Aime 2013) or more complex shapes of occulter (Bout et al. 2000) may improve the performance. We give further analysis on the shape of the penumbra and the shadow cone in Appendix A, for different values of the distance z_0 .

4.3.2. Intensities in plane B

Figure 6 shows the radial intensities $I_B(r)$ in plane B in logarithmic scale. The radial coordinate has been re-scaled in solar unit, and it is limited up to $3.2R_\odot$. Here, the image of the Sun (blue curve) is perfectly focused in the focal plane, and is used as a reference for normalization. It consists of the global response of the raw telescope $S_\emptyset$. The slight decrease in the range $0 - 1R_\odot$ corresponds to the center-to-limb variation. Sunlight falls abruptly to $10^{-3} B_\odot$ at $1R_\odot$, then extends as a large tail of residual light brighter than $10^{-5} B_\odot$. This is due to the summation of the Airy rings at large radius. The diffracted light pattern produced by the external occulter (red curve) consists of a bell-like curve out-of-focus, as expected, since the focal plane is not the image plane with respect to the external occulter. The width of this peak is function of the size of the entrance aperture, in a same way as Airy radius. Note that the peak is not symmetric, and reaches a maximum of $10^{-3} B_\odot$ around $1.05R_\odot$. This last curve modeled the response of the external solar coronagraph S_E.

4.3.3. Intensities in plane O'

Similarly, Figure 7 shows the radial intensities $I_{O'}(r)$ in plane O' in logarithmic scale, using the same scaled axis as Figure 6 for a purpose of comparison. We remind that using solar units here has no real meaning, since plane O' is not conjugated with the Sun as discussed in Section 2.1. The image of the Sun (blue curve) is very similar to the one in the focal plane, but is slightly out-of-focus here, being at $d - f = 0.758$mm ahead. The drop to $10^{-3} B_\odot$ is consequently smoother. The large tail of residual light is still present. As for the diffraction pattern (red curve) made by the external occulter, we obtained a very narrow focused peak of $10^{-2} B_\odot$ amplitude, located at the exact angular position of the edge of the external occulter image, i.e. $1.0568R_\odot$ or 1.629mm. Again, this is expected because plane O' is the image plane of the external occulter. This residual is thus very troublesome at that particular location.

As of now, we already get an idea of the relative difference in the performance of the different coronagraphic systems. In the original Lyot coronagraph S_L, the Lyot mask is set in the focal plane and blocks the direct focused sunlight (blue curve in Figure 6). It will thus let a relatively large amount of residual light propagate further inside the instrument. By adding the external occulter, as in system S_{EL}, the role of the internal occulter is now to block the diffracted light fringe (red curve in Figure 7). Depending where the mask is set, rejection will be more or less efficient. For a purpose of comparison, we looked at the integrated residual light denoted as

$$L(r) = \int_0^{2\pi} d\theta \int_r^{\bar{r}} I_i(r) r dr \tag{15}$$

where $i \in B, O'$, and with the numerical upper limit $\bar{r} = 3.2R_\odot$ already discussed. We analyzed three different cases:

- $L_{S_L}(r)$ the residual light in plane B for the original Lyot coronagraph S_L, without the external occulter
- $L_{S_E}(r)$ the residual light in plane B for the external solar coronagraph S_E, including the external occulter
- $L_{S_{EL}}(r)$ the residual light in plane O' for the hybrid coronagraphic system S_{EL}, including the external occulter

We superimposed in Figure 8 the three residual light curves $L_{S_L}(r)$ (black curve), $L_{S_E}(r)$ (blue curve) and $L_{S_{EL}}(r)$ (red curve), which we normalized. By comparing the residual light from both cases including external occultation, i.e. L_{S_E} and $L_{S_{EL}}$, we can mostly justify the location of the internal occulter for the system S_{EL}. Indeed, it is obvious that the internal occulter, for

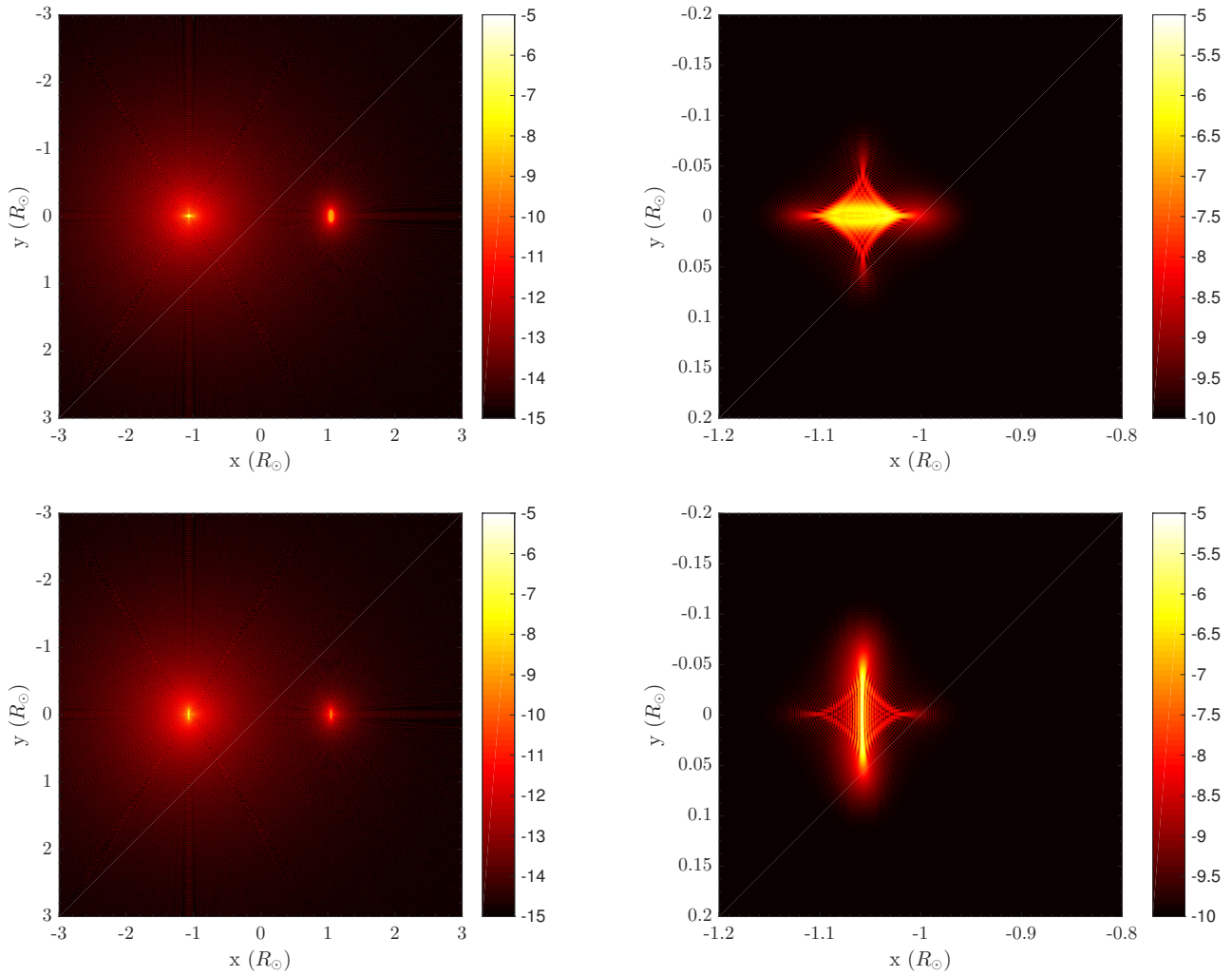

Fig. 4. Two dimension observed intensities of diffracted wave front originating from the off-axis point source at α = 768arcsec, in logarithmic scale. Top: $I_B(x, y)$ in plane B. bottom: $I_{O'}(x, y)$ in plane O'. Both plots on the right zoom in the interesting feature.

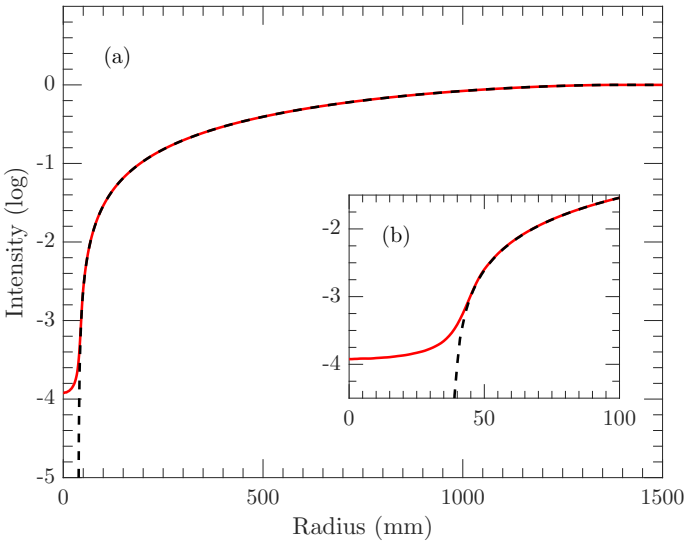

Fig. 5. Intensity $I_A(r)$ on plane A in a logarithmic scale. The intensity is normalized to the mean solar brightness. Red: radial profile of diffracted light produced by the external occulter. Black dashed: related purely geometrical profile. (a) Penumbra profile in full range. (b) Reduced range [0mm; 100mm] corresponding to the umbra region.

a given size, will filter out much more residual diffracted sunlight by being set in plane O' than plane B, because the light is much more focused. The internal occulter must then correctly be set in plane O' when adding the external occulter. At this stage, we can already foresee that the hybrid coronagraphic system S_{EL} will provide the best performance, while keeping a constant vignetting.

4.3.4. Intensities in plane C

Figure 9 presents the radial intensities $I_C(r)$ in plane C in logarithmic scale. The transverse radius is given in mm. A $1.065R_\odot$ Lyot mask and an internal occulter of equivalent angular size have been used here, for the systems S_L and S_{EL} respectively. We normalized the intensities using the exact image of the entrance pupil. The original Lyot coronagraph S_L (blue curve) shows a narrow peak at r = 25mm, being the exact position of the edge of pupil. This $10^{-1}B_\odot$ fringe can be interpreted as a diffraction feature produced by the circular entrance aperture. Similar feature is observed in the case of hybrid coronagraphic system S_{EL} (red curve). The diffraction fringe is however much less bright, reaching about $10^{-4}B_\odot$, due to the external occulter beforehand. The role of the Lyot stop is to crop this diffracted light peak.

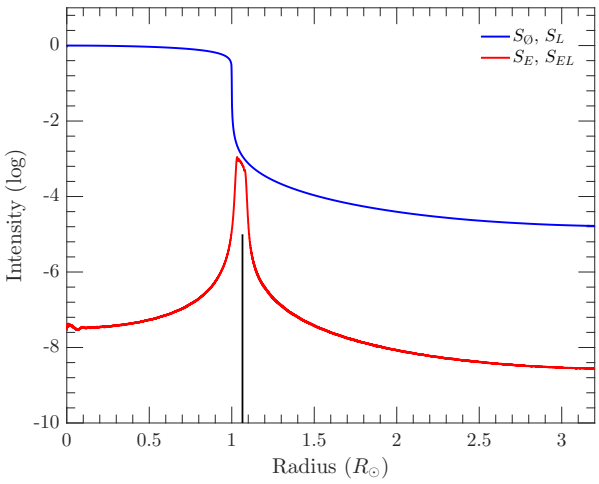

Fig. 6. Observed intensities $I_B(r)$ in plane B in a logarithmic scale. The transverse radius is given in solar units. The intensities are normalized to the mean solar brightness. Blue: response of the raw telescope $S_\emptyset$. Red: response of the external coronagraph S_E. Vertical line: $1.065R_\odot$ radius Lyot mask.

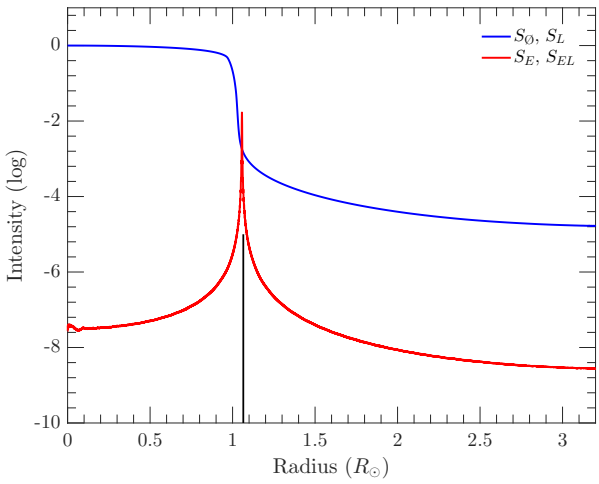

Fig. 7. Observed intensities $I_{O'}(r)$ in plane O' in a logarithmic scale. The transverse radius is given in solar units. The intensities are normalized to the mean solar brightness. Blue: raw image of the Sun in plane O'. Red: systems including the external occulter S_E and S_{EL}. Vertical line: $1.065R_\odot$ radius internal occulter.

4.3.5. Intensities in plane D

Finally, Figure 10 gives the final response of the four imaging systems, in logarithmic scale, using the same occulting masks of $1.065R_\odot$ in planes B and O', and a 24.75mm Lyot stop. We plotted the four observed intensities, meaning $I_B(r)$ for the reference telescope $S_\emptyset$ (black curve) and the external coronagraph S_E (green curve), and $I_D(r)$ for the classic Lyot coronagraph S_L (blue curve) and for the hybrid coronagraphic system S_{EL} (red curve). The reference image of the Sun in plane B is used as a reference for normalization. At the image of the external occulter, both systems S_L and S_E show a relatively high diffraction fringe, being $10^{-3}B_\odot$, while the hybrid coronagraphic system already rejects residual light below $10^{-5}B_\odot$. Outside $1.5R_\odot$, the three systems S_L, S_E and S_{EL} reject below $10^{-6}B_\odot$, $10^{-7}B_\odot$ and $10^{-8}B_\odot$ respectively. As for now, this analysis has proved the efficiency of the combination of an external occulter with a Lyot coronagraph. While the classic Lyot coronagraph seems to be the less efficient, the externally occulted hybrid coronagraph S_{EL} provides the best performance in terms of stray ligth rejection, with a gain of at least two orders of magnitude.

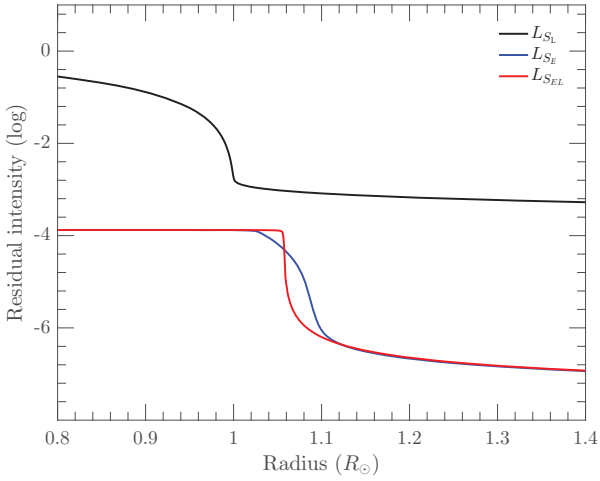

Fig. 8. Integrated residual light $L(r)$, as given in Eq.(15), in logarithmic scale, and normalized to $L_{S_L}(0)$. Zoom in the range $[0.8R_\odot, 1.4R_\odot]$. Black: L_{S_L}. Blue: L_{S_E}. Red: $L_{S_{EL}}$.

4.4. Sizing the internal occulter and the Lyot stop

Based on the configuration of the coronagraphic system S_{EL}, we now investigate the impact of sizing the internal occulter, keeping the external occultation ratio R/z_0 constant. We computed the response in plane D for several sizes of internal occulter set in plane O'. We looked at radii of 1.005, 1.01, 1.02, 1.03 and 1.04 times the external occulter image. They respectively corresponds to radii of 1.637mm ($1.0621R_\odot$), 1.645mm ($1.0674R_\odot$), 1.662mm ($1.0779R_\odot$), 1.678mm ($1.0885R_\odot$) and 1.694mm ($1.0991R_\odot$). We superimposed in Figure 11 the radial cuts of intensities $I_D(r)$, in logarithmic scale, using a Lyot stop of 24.75mm radius (plot on the left) and one of 24mm radius (plot on the right). The plot is given in the range $0.5-2R_\odot$ to highlight the diffraction fringe area.

In a similar way, we analyzed the effect of reducing the Lyot stop, keeping a fixed internal occulter. We compared in Figure 12 the radial cuts of final intensities $I_D(r)$, in logarithmic scale, using internal occulters of 1.01 (plot on the left) and 1.03 external occulter image (plot on the right). We used Lyot stops of 25mm, 24.75mm, 24.50mm, 24mm, and 23mm radius. The interested reader will find in Appendix B the same study for the original Lyot coronagraph.

As a global result, we show here that the Lyot stop mainly acts over the residual light in the range $1.2-3R_\odot$, and does not impact significantly the main diffraction feature. Reducing the radius of the Lyot stop from 25mm to 24.75mm already gives appreciable improvement, of about one order of magnitude. In parallel, oversizing the internal occulter mainly contributes to reducing the level of residual sunlight around the edge of the external occulter image. The decrease is not linear, and we can roughly estimate an improvement of two orders of magnitude from 1.005 to 1.02 external occulter image radius. The rising question is then to deal with vignetting, which controls the spatial resolution in the inner part of the solar corona. Yet, we did

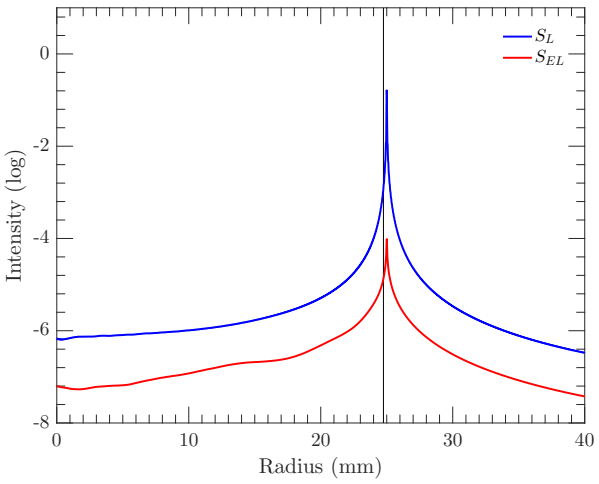

Fig. 9. Observed intensities $I_C(r)$ in plane C in a logarithmic scale. The transverse radius is given in mm. The intensities are normalized to the mean solar brightness. Blue: system S_L. Red: system S_{EL}. Vertical line: 24.75mm radius Lyot stop.

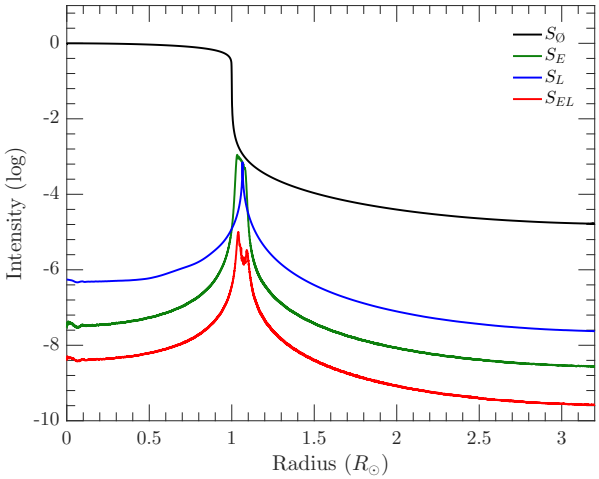

Fig. 10. Final response as observed intensities in the focal plane in a logarithmic scale. The transverse radius is given in solar units. The intensities are normalized to the mean solar brightness. Black: system $S_\emptyset$ given by $I_B(r)$ in plane B. Blue: system S_L given by $I_D(r)$ in plane D. Black: system S_E given by $I_B(r)$ in plane B. Red: system S_{EL} given by $I_D(r)$ in plane D.

not look at detailed vignetting functions in our present work. Finally, we want to emphasize that the residual light in the range $1.5 - 3.2R_\odot$ is more impacted by the size of the Lyot stop than the internal occulter.

de Lyot It is of course the combined effect of the internal occulter and the Lyot stop that makes the performance of the coronagraph. Figure 13 illustrates this point by plotting the residual scattered sunlight level observed at $1.3R_\odot$, as function of the radius of the internal occulter and of the Lyot stop the Lyot stop. The region $1.3R_\odot$ has been arbitrarily chosen. At least, it seems that such a coronagraphic system theoretically manages to reject below $10^{-8}B_\odot$ using a $1.065R_\odot$ internal occulter, which is 1.05 times the external occulter image. Even more, a performance of $10^{-10}B_\odot$ at $1.3R_\odot$ looks feasible at the price of increasing the inner vignetting of the instrument. So, combining this assessment with a fine analysis of the vignetting function of the instrument will allow a complete theoretical performance study of the resolution of the coronagraphic system.

5. Conclusions

We presented a dedicated numerical analysis to compute the theoretical performance of different solar coronagraphic systems. Starting with Fresnel diffraction induced by the external occulting disc, we investigated the propagation of the wave front inside the Lyot coronagraph. We compared the external solar coronagraph, the original Lyot coronagraph with a Lyot mask alone and the hybrid externally occulted Lyot solar coronagraph, using the geometrical parameters of ASPIICS. With a Lyot mask of $1.065R_\odot$ radius and a Lyot stop of 24.75mm radius, the original Lyot coronagraph rejects below $10^{-6}B_\odot$ around $1.5R_\odot$, but the residual diffracted sunlight remains brighter than $10^{-8}B_\odot$ outside $1.5R_\odot$. The external coronagraph alone manages to gain one order of magnitude, while the hybrid cornagraphic system achieves a stray light rejection below $10^{-8}B_\odot$ outside $1.5R_\odot$, using the same configuration. The performance for such a cornagraph looks more efficient compared to the classic Lyot coronagraph, thanks to the external occultation.

We refined our study to exhibit the coupled effects of sizing both internal occulter and Lyot stop. Oversizing the mask enables to decrease the intensity of the diffraction fringe located at the image of the external occulter, while reducing the radius of the stop allows to globally reduce the residual light outside this peak. As a concrete result, we provided in figure 13 a graph that allows simply estimating the performance, given at $1.3R_\odot$, as a function of sizes of the internal occulter and Lyot stop. We showed that it is feasible to reject below $10^{-8}B_\odot$ using an internal occulter whose radius is smaller than $1.07R_\odot$. However, achieving a rejection below $10^{-10}B_\odot$ is very demanding in over occultation. This last analysis shall be coupled to a fine study of the vignetting function of the instrument. However, we would like to emphasize that our results remain purely theoretical, since our computation is based on the assumptions of perfect optics and alignment. The introduction of other sources of scattering, such as ghost, bulk scatter or wave front errors of the optics, may degrade the present performance.

If the predominant diffraction features remains troublesome, one can investigate in the nature of the external occulting disc itself. Apodization techniques applied to external occulters have already been analytically proved by Aime (2013) to be more efficient than the simple sharp-edged disc we considered here. What naturally follows this work consists in the study of more complex type of occulters and related analytic performance. Numerical optimization can be also further investigated, as it has already been done for exoplanet coronagraphy, like the work of Flamary (2014). The main difficulty yet stands in the two dimensional representation of such complex shapes and computing the analytic expression of Fresnel diffraction.

It would be interested to confront our analysis to experimental studies of stray light rejection. The approach described by Venêt et al. (2010) or the dedicated measurements and optimization of ocuclting disc presented by Landini et al. (2010) shall provide quantitative data about relative gains of different types of occulters to be coupled with the theoretical analysis of performance for the hybrid externally occulted Lyot coronagraph.

Acknowledgement We would like to thank the support of the European Space Agency and Proba-3 project for having largely supported this activity.

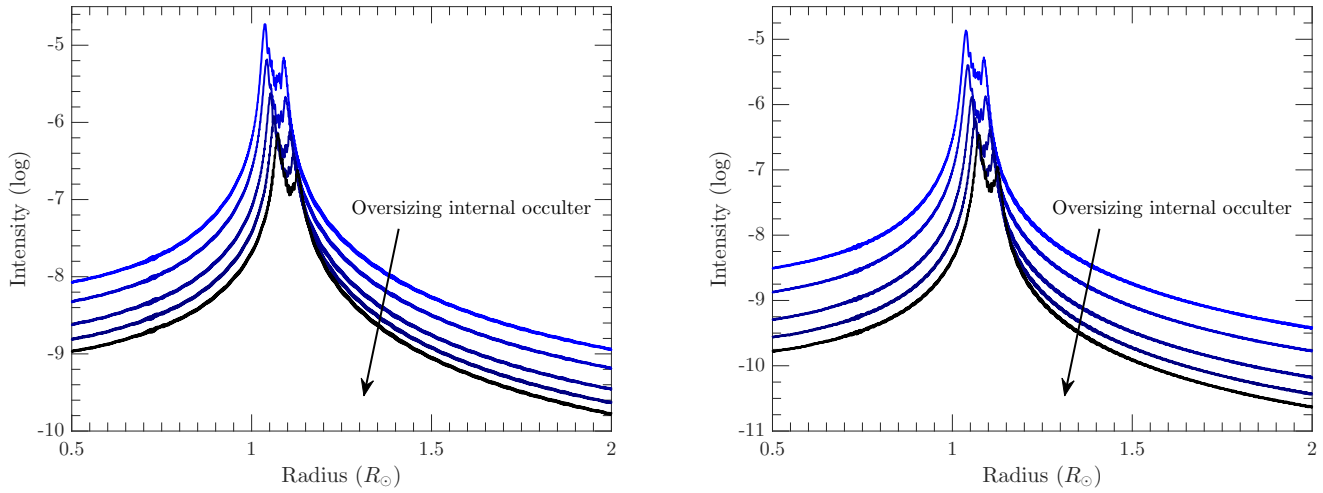

Fig. 11. Radial cuts $I_D(r)$ for internal occulters of 1.005, 1.01, 1.02, 1.03 and 1.04 external occulter image, in logarithmic scale. Left: fixed Lyot stop of 24.75mm radius. Right: fixed Lyot stop of 24mm radius. The transverse radius is given in solar units, in the range $[0.5R_\odot, 2R_\odot]$. The intensities are normalized to the mean solar brightness.

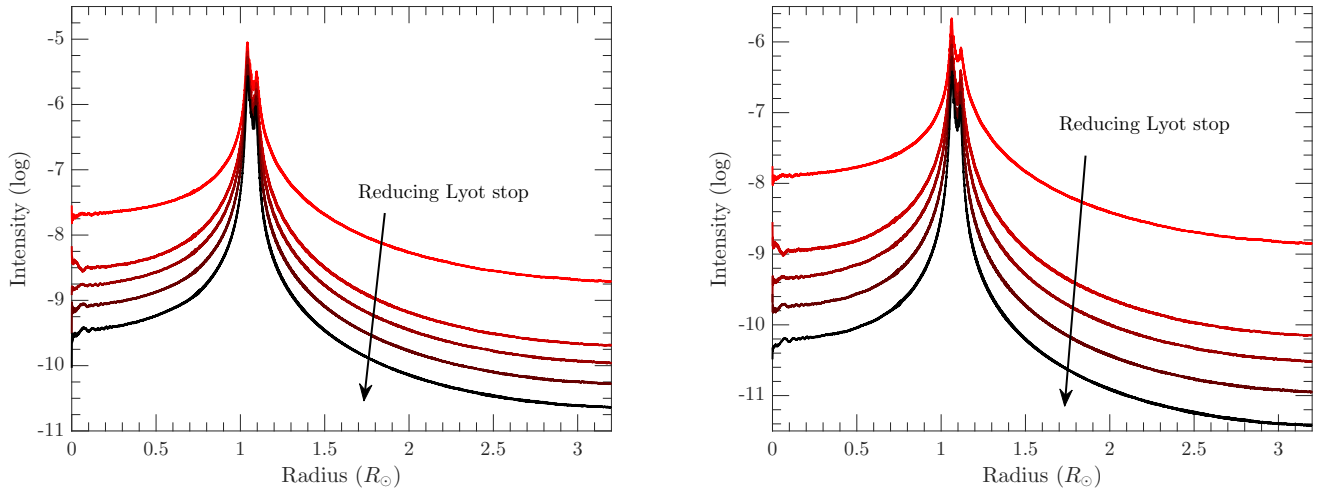

Fig. 12. Radial cuts $I_D(r)$ for Lyot stops of 25mm, 24.75mm, 24.50mm, 24mm and 23mm radius, in logarithmic scale. Left: fixed internal occulter of 1.01 external occulter image. Right: fixed internal occulter of 1.03 external occulter image. The transverse radius is given in solar units. The intensities are normalized to the mean solar brightness.

References

Aime, C., Soummer, R., & Ferrari, A. 2002 A&A, 389, 334
Aime, C. 2013, A&A, 558, 138
Cox, A. N. 2000, Allen's astrophysical quantities
Born, M., & Wolf, E. 2006 Principles of Optics, 7th edn.(Cambridge University Press), 484
Bout, M., Lamy, P., Maucherat, A., Colin, C. & Llebaria, A. 2000 Appl. Opt., 39, 22
Brueckner, G. E. Howard, R. A., Koomen, M. J. et al. 1995 Solar Phys., 162, 357
Dollfus, A. 1983, L'Astronomie, 97, 107-129
Evans, J. W. 1948, Science Sci. Rev., 47, 95
Flamary, R. and Aime, C. 2014, A&A, 569, A28
Fort, B., Morel, C., & Spaak, G. 1978 Astron. Astrophys. 63, 243
Galy, C. 2015, SPIE, vol. 9604, 96040B
Goodman, J. W. 2005, Introduction to Fourier Optics (Roberts and Company Publishers)
Hamme, V. 1993 Astron. J., 106, 5
Koutchmy, S. 1988, Science Sci. Rev., 47, 95
Landini, F. et al. 2010, SPIE, vol. 7735, 77354D
Lemoine, D. 1994, J. Chem. Phys., 101, 3936
Lamy, P., Damé, L., Vivès, S., & Zukhov, A. 2010, SPIE, 7731, 18
Lyot, B. 1939, MNRAS, 99, 580
Newkirk, G., Jr. & Bohlin, D. 1965 Ann. Astrophys. 28, 234
Purcell, J. D., & Koomen, M. J. 1962 in Report of NRL Progress, US GPO, Washington D.C., p.9
Renotte, E., et al. 2015, SPIE, 9604, 96040A
Soummer, R., Pueyo, L., Sivaramakrishan, A., & Vanderbei, R. J, 2007 Optics Express, vol. 15, issue 24, p. 15935
Venêt, M., Bazin, C., Koutchmy, S., & Lamy, P. 2010 ICSO 2010
Verroi, E., Frassetto, F., & Naletto, G. 2008 J. Opt. Soc. Am. Am 25, 182
Wolfram 2012, Mathematica (Champaign, IL: Wolfram Research, Inc.)

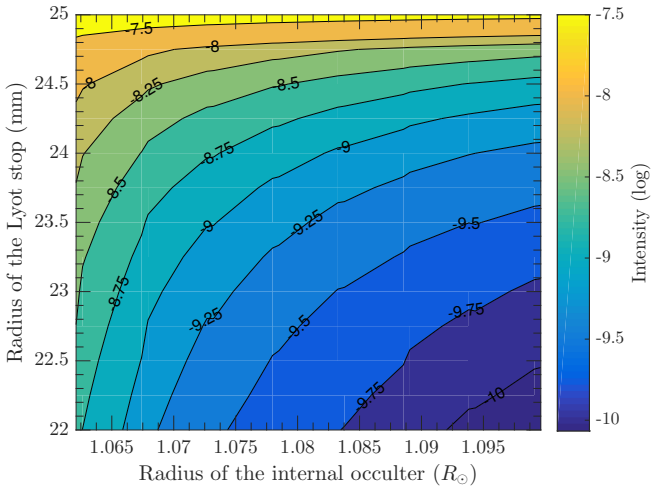

Fig. 13. Residual scattered sunlight level at $1.3R_\odot$ for system S_{EL}, in logarithmic scale. The horizontal axis represents the radius of the internal occulter set in O', in $R_\odot$ units. The vertical axis represents the radius of the Lyot stop set in plane C, in mm.

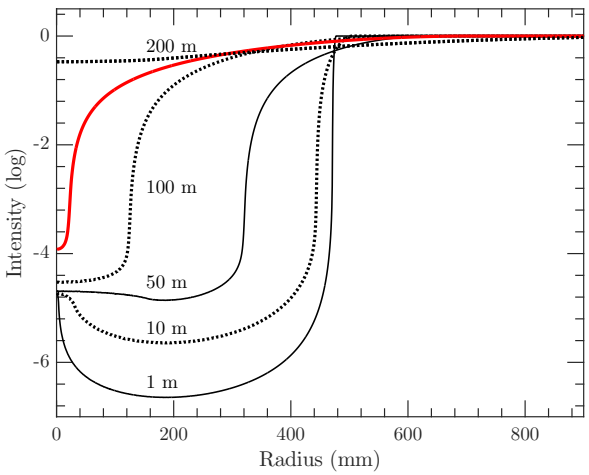

Fig. A.1. Intensity $I_A(r)$ on plane A in a logarithmic scale. The intensity is normalized to the mean solar brightness. From top to bottom: z_0 = 1m, 10m, 50m, 100m, 144.348m and 200m. The red curve corresponding to ASPIICS nominal geometry. The curves are normalized to the mean solar brightness $B_\odot$.

Appendix A: Study of the penumbra cone by varying the distance z_0

The shape of the umbra cone is intimately linked to the distance z between the external occulter and the aperture of the telescope. In the context of Proba-3 Formation Flying mission, this has a particular interest, since the inter spacecraft distance between the Coronagraph and the Occulter may vary. We computed the Fresnel diffraction pattern Eq.(5) and the penumbra profile in plane A $I_A(r)$ given by Eq.(12) for different values of z_0, keeping the same parameters for the external occulter, the Sun and the wavelength.

In Fig.A.1 we give the radial penumbra profile of diffracted light in logarithmic scale at z_0 = 1m, 10m, 50m, 100m, 144.348m and 200m. Before all, we must advertise that Fresnel diffraction theory may not be fully justified at small z_0 as the approximation of small angles is no more valid. The smaller z_0, the smaller the stenope image of the Sun in plane O, computed as $z_0 \tan R_\odot$, as given in Table A.1. So, at $z_0 \leq$ 50m, the radial penumbra profile shows a bell-shape in the central region, due to the two dimension convolution of this stenope image with the Arago bright spot in plane A. At larger z_0, this feature vanishes and we obtain a smooth penumbra profile. We notice that the umbra is about 2, 5 darker at z_0 = 100m than 144.348m, as plane A is then closer to the occulter, with a larger radius of mm. The geometrical umbra is reduced to a point at z_0 = 152.55m, and the so-called ante-umbra region extends behind, as the external occulter cannot mask the whole solar disc, as illustrated by the case z_0 = 200m in Fig.A.1.

Appendix B: Reducing the Lyot stop for the original Lyot coronagraph

We report in this appendix the study of reducing the Lyot stop for the classic Lyot coronagraph S_L. The approach is the same as the one presented in Section 4.4. We computed the global response in the final focal plane of the coronagraph by varying the radius of the Lyot stop, from 25mm to 24mm, using a fixed $1.065R_\odot$ Lyot mask set in plane B. We also investigated the case without Lyot stop in plane C. Figure B.1 shows the results $I_D(r)$.

Table A.1. Relations between distance z_0 between the external occulter and plane A, stenope image radius of the Sun in plane O and geometrical radius of the umbra. **(*)**: the geometrical umbra does not exist since the solar disc is no more fully masked by the occulting disc.

z_0	Solar stenope image	Geometrical umbra
1 m	4.65 mm	705 mm
10 m	46.5 mm	633 mm
50 m	233 mm	477 mm
100 m	465 mm	240 mm
144.348 m	672 mm	38 mm
200 m	931 mm	**(*)**

the contribution of reducing the Lyot stop is clear, with a gain of three orders of magnitude around $2R_\odot$ in rejection of residual diffracted sunlight.

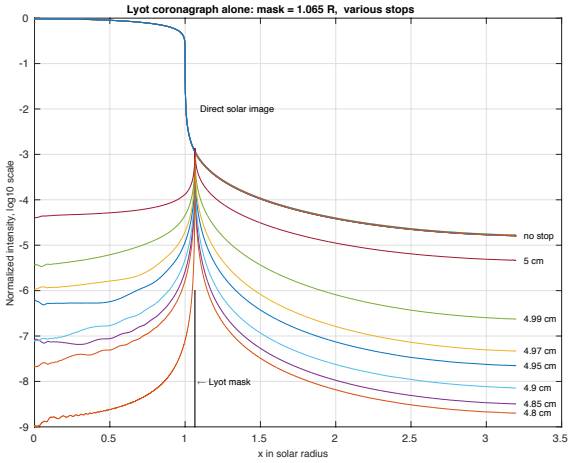

Fig. B.1. Radial cuts $I_D(r)$ for the classic Lyot coronagraph S_L, in logarithmic scale. From top to bottom: no Lyot stop, Lyot stop of 25mm, 24.95mm, 24.85mm, 24.75mm, 24.45mm, 24.25mm and 24mm radius. The transverse radius is given in solar units. The intensities are normalized to the mean solar brightness.

Appendix C: Two dimension intensities

In this appendix, we report the two dimension image of the global response related to the four different imaging systems studied. Figure C.1 plots $I_B(x, y)$ in plane B for the raw telescope $S_{\emptyset}$ and the external coronagraph S_E, and $I_D(x, y)$ in plane D for the Lyot coronagraph S_L and the hybrid coronagraphic system S_{EL}. A $1.065R_{\odot}$ radius Lyot mask or internal internal and a 24.75mm radius Lyot stop have been used for the computation. The same color logarithmic scale has been set to every plots for a purpose of direct comparisons.

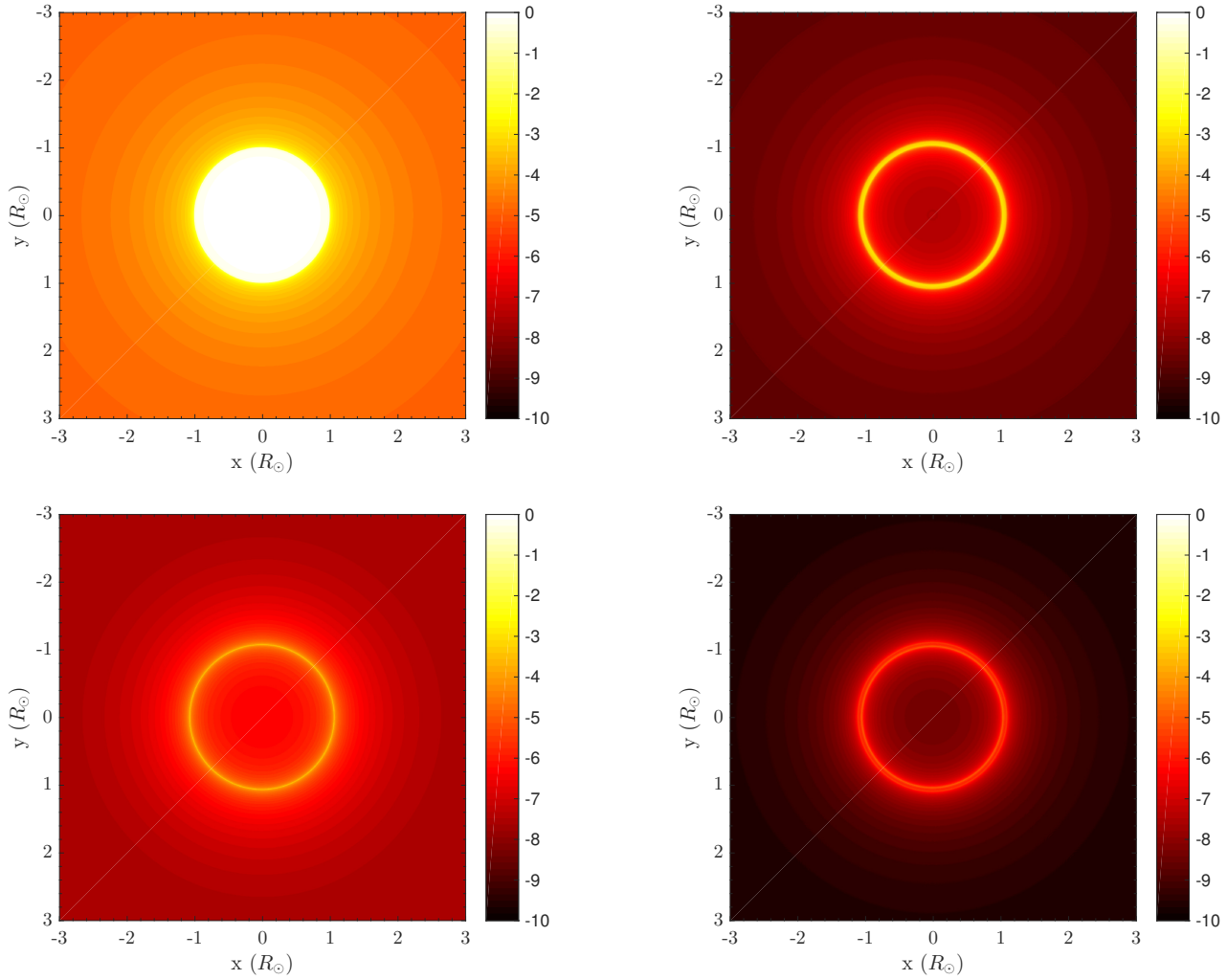

Fig. C.1. Two dimensions observed intensities in the detection plane, i.e. plane B for systems $S_{\emptyset}$ and S_E and plane D for systems S_L and S_{EL}, in logarithmic scale. The intensities are normalized to the mean solar brightness. Top left: system $S_{\emptyset}$. Top Right: system S_E. Bottom left: system S_L. Bottom right: system S_{EL}.